Renewable Energy 221 (2024) 119767

Contents lists available at ScienceDirect

Renewable Energy

journal homepage: www.elsevier.com/locate/renene

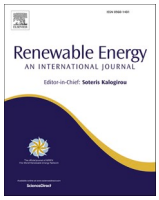

Exploring a novel tubular-type modular reactor for solar-driven thermochemical energy storage

Yong Zhang, Mingke Hu *, Ziwei Chen, Yuehong Su **, Saffa Riffat

Department of Architecture and Built Environment, University of Nottingham, University Park, Nottingham, NG7 2RD, UK

ARTICLE INFO

Keywords:
Thermochemical energy storage
Tubular-type modular reactor
Discharging
Equivalent thermal efficiency
Pressure drop

ABSTRACT

Thermochemical energy storage (TCES) has gained extensive attention as a potential solution to address the mismatch between solar thermal energy production and demand. In this study, a novel tubular-type modular TCES reactor is introduced. COMSOL modelling of the system is developed and experimentally validated using a laboratory-scale TCES system. Both types of reactors show similar temperature increases, intensifying with higher inlet relative humidity. Their maximum temperature lifts exceeding 26 °C at 90 % RH. Tubular designs offer better axial flexural strength and dispersion of TCES composite materials compared to plate structures. This property of tubular structures beneficial reducing bed thickness and pressure drop and enhancing equivalent thermal efficiency. Simulations show tubular-type modular reactors reduce pressure drop by 4–5 times compared to plate-type modular reactors, increasing equivalent thermal efficiency by nearly 7% points. Increasing the number of reactor beds and inner tube radius improves equivalent thermal efficiency due to reduced bed thickness and pressure drop. As the number of matrix rows and columns in the reactor bed increases from 2 to 10, bed thickness decreases from 0.058 m to 0.012 m, reducing pressure drop from 845.53 Pa to 38 Pa and increasing equivalent thermal efficiency from 78.82 % to 96.61 %.

1. Introduction

Currently, the United Kingdom is facing an unprecedented energy crisis [1]. To help UK households overcome the energy crisis, one effective approach is to increase the utilisation of renewable energy sources for residential heating, particularly solar energy [2]. However, the intermittent nature of solar energy hinders its development [3]. Thermal energy storage (TES) technology provides a promising solution to address the imbalance between the heat supply from solar collectors and the heating demand in buildings [4]. TES can be classified into three categories: sensible thermal energy storage (STES) [5], latent thermal energy storage (LTES) [6], and thermochemical energy storage (TCES) [7]. Among these, TCES offers a higher energy storage density (approximately 200–700 $kWh \cdot m^{-3}$) compared to the other two technologies [2]. Additionally, the thermal energy in TCES systems is stored in the form of chemical potential, resulting in negligible thermal energy losses during long-term storage [8]. Salt hydrates have attracted attention as thermochemical materials (TCMs) due to their high energy storage density [9], non-toxic nature [10], and low charging temperatures [11].

Salt hydrate-based TCES systems can be categorized into two types: open TCES systems and closed TCES systems [12], the schematic diagrams of these two systems are presented in Fig. 1. In an open TCES system, the direct dehydration of salt hydrates occurs in the high-temperature airflow originating from the heat source during the charging process, enabling the conversion of thermal energy into chemical potential. Concurrently, water vapor is emitted into the external environment. In the discharging process, water molecules present in the humidified air are absorbed by the dehydrated salts, resulting in the formation of salt hydrates. Simultaneously, the chemical potential is reconverted back into thermal energy, heating the airflow passing through the system for space heating purposes. In an open TCES system, water vapor not only acts as the reactant product in the reversible solid-gas reactions [13] but also serves as the medium for heat and mass transfer in TCES systems, eliminating the requirement for additional components [14]. This open configuration offers advantages in terms of structure, volumetric energy density, cost, and efficiency [15–17].

* Corresponding author.
** Corresponding author.
E-mail addresses: mingke.hu@nottingham.ac.uk (M. Hu), yuehong.su@nottingham.ac.uk (Y. Su).

https://doi.org/10.1016/j.renene.2023.119767
Received 14 August 2023; Received in revised form 29 October 2023; Accepted 28 November 2023
Available online 2 December 2023

In contrast, closed TCES systems employ a closed gas loop isolated from the ambient. During the charging process, heat is typically transferred to the salt hydrate and makes it dehydrate through a heat exchanger, and the desorbed water vapor subsequently liquefies in a condenser. During the discharging process, water vapor from the evaporator causes the salt to revert to salt hydrate, and the released heat from the salt hydration reaction is transferred to an internal heat exchanger connected to the building for space heating. The closed TCES system requires a humidifier and a dehumidifier to generate and collect water vapor during both discharging and charging processes, as well as heat exchanger units for heat transfer to external applications [18]. Additionally, closed systems necessitate a reactor with high vacuum and sealing integrity, making them more complex and costly [19]. On the other hand, closed systems offer the advantage of minimal environmental pollution owing to their excellent sealing integrity [20]. Considering the environmental friendliness of salt hydrates, open-cycle configurations are more commonly utilized in salt hydrate-based TCES systems [21].

In salt hydrate-based TCES systems, the low deliquescence relative humidity characteristic of pure salts makes them prone to deliquescence and agglomeration during the discharging process, posing challenges for heat and mass transfer in the reactor and limiting the discharging performance [22]. Currently, two main approaches are employed to address these issues. The first approach involves impregnating salt hydrates into a porous matrix (e.g., silica gel [23], zeolite [24], vermiculite [2], expanded graphite [25], activated alumina [26], bentonite clay [27] and ceramic foam [28]) to form TCES composite materials [19], which combine the advantages of both salt hydrates and porous materials while mitigating their respective drawbacks [13]. The numerous micrometre-sized pores in TCES composite materials facilitate gas diffusion and promote mass transfer, thereby reducing salt aggregation and melting during discharging process [20]. Although these composite materials have demonstrated promising performance and applicability, their energy storage density and durability still require further development and improvements [13,28,29].

The second approach focuses on optimising the reactor's structure to enhance the mass and heat transfer performance of TCES reactors. Researchers have explored various reactor designs as alternatives to traditional packed beds, such as honeycomb configurations [30], multi-module setups [31], serially connected modules [32], and the use of copper mesh fillers [33]. These reactor configurations aim to optimise heat and mass transfer within the system and ultimately enhance overall system performance. However, recent literature reviews have revealed a significant oversight in the field, where limited attention has been given to the crucial aspect of the structural optimisation in open salt hydrate reactors. In most studies on open TCES systems, TCMs are simply placed in one or more rectangular-shaped reaction beds. Nevertheless, these conventional reactor beds are plagued by substantial pressure drops, not only resulting in excessive airflow resistance and the potential reduction in mass transfer coefficient, but also impose an additional challenge of increased fan power consumption.

To tackle these technical challenges, our present work proposes a novel TCES reactor design incorporating perforated tubular-type modular reactor beds aimed at reducing pressure drop and improving system equivalent thermal efficiency. In this study, a mathematical model of the proposed TCES reactor is established in COMSOL software and validated experimentally with a lab-scale TCES reactor test rig. A numerical study is conducted to compare the performance of the tubular-type modular reactor with a traditional plate-type modular reactor at different inlet conditions The impacts of different structural parameters of the tubular-type modular reactor on the thermal performance of the TCES system are also evaluated. This work contributes to the field by presenting a comprehensive numerical analysis of an improved TCES reactor design, which provides insights into its operational mechanisms and potential applications for thermochemical energy storage.

2. System description

A 3D tubular-type modular TCES reactor model was developed, consisting of 64 tubular-type modular reaction beds. The reactor's cross-sectional view along the centre axis is presented in Fig. 2. The reactor is a cube with a side length of 0.4 m and has channels as the inlet and outlet for airflow on the left and right ends, respectively. Each modular reaction bed comprises an outer and inner perforated cylindrical shell, with TCES composite materials filling the space between them. In this numerical study, the selected composite material is vermiculite impregnated with calcium chloride ($CaCl_2$), referred to as vermiculite- $CaCl_2$. The basic structure and working principle are depicted in Fig. 2. The outer perforated pipe has a length and diameter of 0.4 m and 0.05 m,

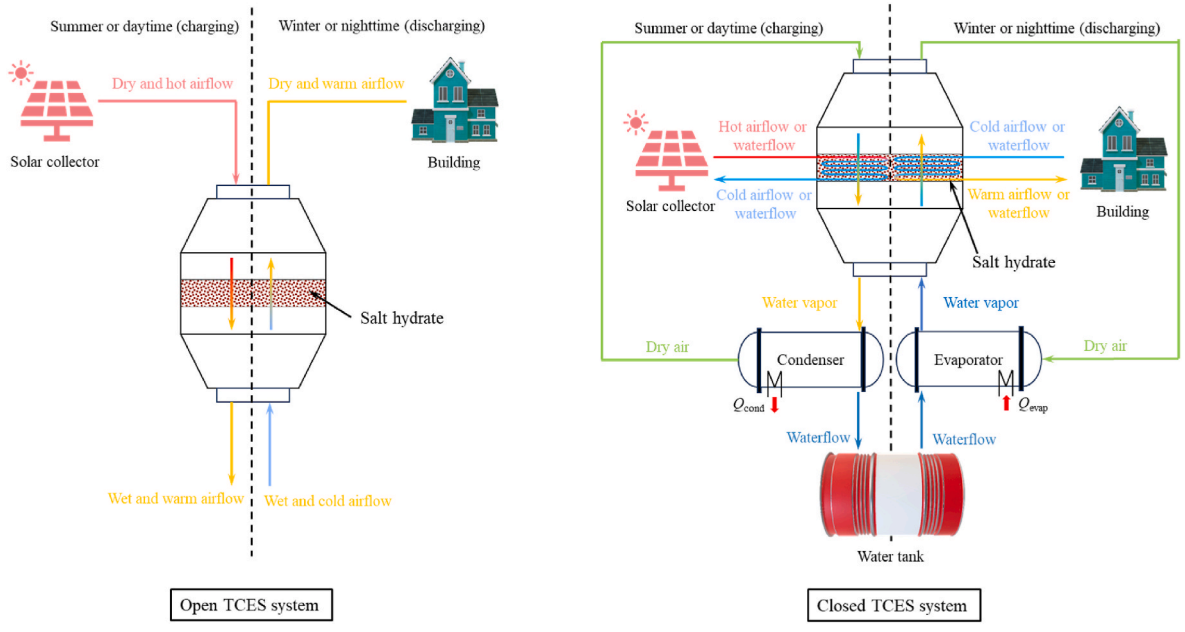

Fig. 1. Schematic diagrams of open and closed salt hydrate-based TCES systems.

respectively, while the inner perforated pipe has a length and diameter of 0.385 m and 0.02 m, respectively. Each modular reaction bed can store 0.66 L of TCES composite materials, resulting in a total TCES composite materials storage capacity of 42.50 L for the entire reactor.

This numerical study focuses on the discharging process. As illustrated in Fig. 2, during the discharging process, the moist and cold air enters the air channel formed by the inner perforated pipe from the open end at the left of the reaction bed upon entering the reactor through the inlet. The air then diffuses uniformly into the TCES composite materials through the holes in the inner perforated pipe, where the TCES composite materials absorb moisture and release heat, thereby increasing the air temperature. The heated air then diffuses outward and exits the reaction bed through the holes in the outer perforated pipe, entering the air channel between the modular reaction beds. Finally, the air leaves the reactor through the reactor outlet.

During the charging process, the reactant $CaCl_2 \bullet 6H_2O$ in the vermiculite-$CaCl_2$ composite, absorbs heat from a heat source (e.g., a solar collector). This leads to the decomposition of $CaCl_2 \bullet 6H_2O$ into two products (i.e., $CaCl_2$ and H_2O), wherein the absorbed heat is transformed into stable chemical potential energy stored within the vermiculite-$CaCl_2$ composite. Reversibly, when $CaCl_2$ comes into contact with water vapor or moist air, the stored chemical potential energy is converted back into thermal energy, leading to the heating of the heat transfer medium (e.g., air or water). The schematic diagram of the charging and discharging processes is provided in Fig. 3, and the reversible chemical reaction can be described as follows [34]:

$$CaCl_2 \cdot 6H_2O_{(solid)} + 6\Delta H \underset{\text{Discharging}}{\overset{\text{Charging}}{\rightleftarrows}} CaCl_{2(solid)} + 6H_2O_{(gas)} \quad \Delta H = 53.4\ \text{kJ} \cdot \text{mol}^{-1} \tag{1}$$

To compare the discharging performance between the tubular-type modular reactor and the plate-type modular reactor, a model of the plate-type modular reactor was developed using COMSOL, and its 3D structure is depicted in Fig. 4. The external dimensions of the plate-type modular reactor match those of the tubular-type modular reactor. Internally, it comprises eight reaction beds, each with dimensions of 400 mm × 400 mm × 33 mm (length × width × height). The spaces between the reaction beds form four air inlet channels and five air outlet channels, each with a height of 15 mm, and their channel ends are sealed. Moist air is directed into the inlet channel and then compelled to traverse the reactor bed, either upward or downward, before exiting through the outlet channel. Eventually, it exits the reactor and disperses into the extern of the reactor.

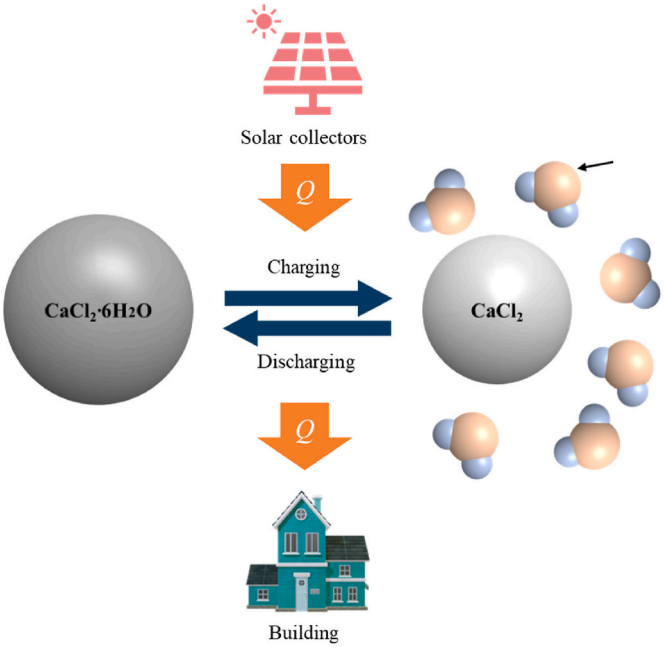

Fig. 3. Schematic diagram of the charging and discharging process of the salt hydrate as TCES material.

2. Mathematical model

This section presents a developed mathematical model aimed at quantitatively assessing the discharging performance of the proposed tubular-type modular TCES reactor. The numerical investigation incorporates several assumptions to establish control equations describing the mass and energy transfer processes within the TCES system.

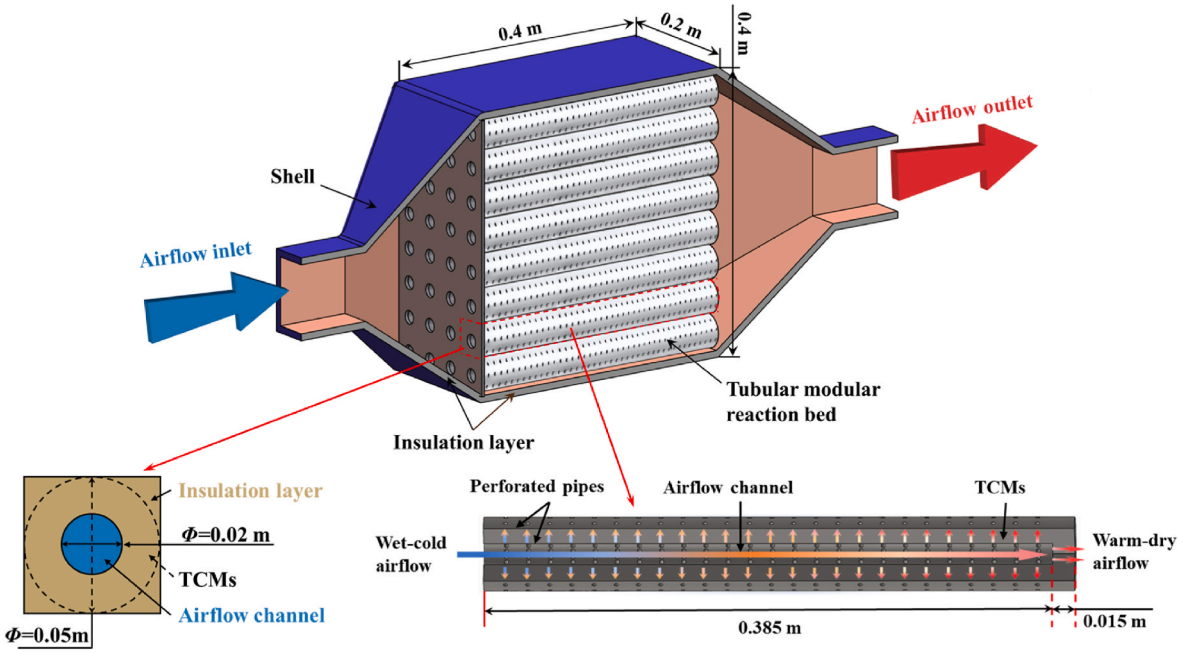

Fig. 2. 3D cross-sectional schematic diagram of the tubular-type modular TCES reactor and illustration of the tubular-type modular reaction bed.

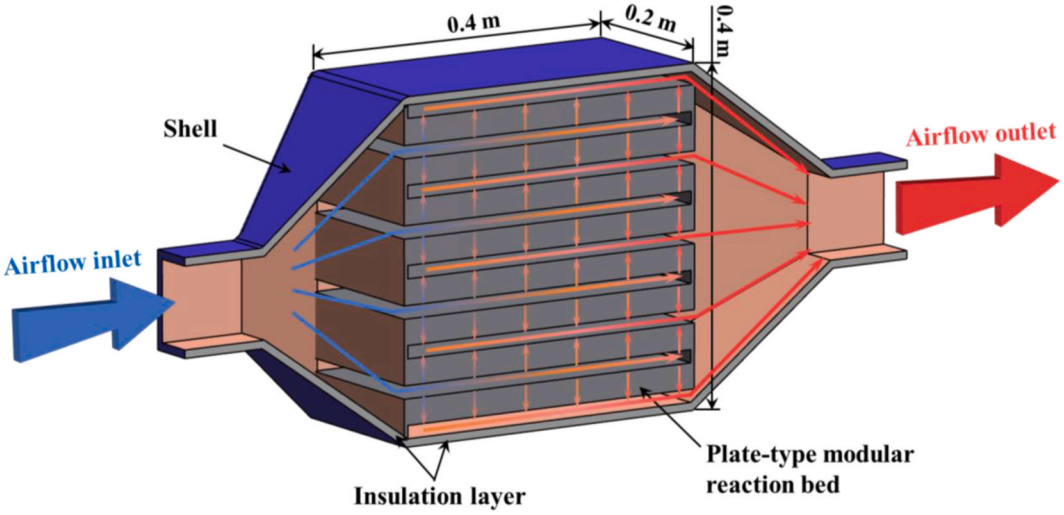

Fig. 4. 3D cross-sectional diagram of the plate-type modular reactor.

1. Local thermal equilibrium between TCES composite materials and the airflow within the reaction bed [4,17].
2. Neglecting the radiative heat transfer effects within the reactor [35,36].
3. Considering the airflow as an ideal gas and uniform distribution within the reaction bed, following Dalton's law [37].
4. Uniform dispersion of TCES composite materials throughout the entire reaction bed, excluding the influence of sieve plates on the solid-gas reaction [38].

3.1. Reaction kinetics

The conversion rate of salt hydrates in TCES composite materials can be characterized by three main variables: the conversion degree α, the pressure P, and the thermodynamic temperature T. The kinetics of the hydration reaction of the dehydrated salt and the dehydration reaction of salt hydrates can be mathematically expressed as follows [35]:

$$\frac{\partial \alpha}{\partial t} = R_{kin}\alpha\left(1-\frac{p_v}{p_{eq}}\right) = A_{freq}\exp\left(-\frac{E_a}{RT}\right)\alpha\left(1-\frac{p_v}{p_{eq}}\right) \quad \text{for discharging} \tag{2}$$

where α is the conversion degree; R_{kin} is the chemical kinetic factor, s^{-1}; p_v and p_{eq} are the partial pressure of water vapor and the equilibrium pressure of water vapor, respectively, Pa; A_{freq} is the pre-exponential Arrhenius factor, s^{-1}; R is the ideal gas constant, kJ•mol^{-1}•K^{-1}, and E_a refers to the Arrhenius activation energy, kJ•mol^{-1}.

The conversion degree α represents the extent of transformation from salt hydrate to dehydrated salt in the reversible solid-gas thermochemical reaction. During charging, the salt hydrate dehydrates at high temperatures, converting into dehydrated salt ($\alpha = 0 \rightarrow \alpha = 1$). In the discharging process, the dehydrated salt absorbs moisture and reverts back to salt hydrate ($\alpha = 1 \rightarrow \alpha = 0$). The conversion degree can be defined as [39]:

$$\alpha(t) = \frac{m_{s,i} - m_s(t)}{m_{s,i} - m_{s,f}} \tag{3}$$

where $m_{s,i}$ and $m_{s,f}$ are respectively the initial and final mass of the salt hydrate (i.e., $CaCl_2$•$6H_2O$) in the reaction bed, kg. Given that the utilized model in COMSOL exclusively considers concentration, the expression for the degree of conversion has been accordingly modified to Ref. [40]:

$$\alpha(t) = \frac{c_{s,i} - c_s(t)}{c_{s,i} - c_{s,f}} \tag{4}$$

where $c_{s,i}$ and $c_{s,f}$ are the initial and final molar concentration of the salt hydrate, mol•m^{-3}, respectively.

Assuming that the mass transfer and chemical reactions during the solid-gas reaction occur rapidly enough to maintain the system at a relatively stable temperature, the equilibrium pressure (p_{eq}) and temperature (T) are considered to follow the relationship described by the Clausius-Clapeyron equation, which is given by:

$$\ln\left(\frac{p_{eq}}{p_{ref}}\right) = -\frac{\Delta H_r}{RT} + \frac{\Delta S_r}{R} \tag{5}$$

where p_{ref} is the reference pressure, Pa; ΔH_r is the reaction enthalpy, kJ•mol^{-1}; and ΔS_r is the reaction entropy, kJ•mol^{-1}•K^{-1}.

2.2. Mass conservation

During the charging process of the TCES system, the salt hydrate undergoes a dehydration reaction, resulting in an increase in the mass density of water vapor. However, during the discharging process of the TCES system, the absorption of moisture by the dehydrated salt leads to a reverse change in the mass density of water vapor. Considering the porosity of the reaction bed, the mass balance equation for water vapor can be expressed as follows:

$$\varepsilon\frac{\partial \rho_v}{\partial t} = S_w - \nabla(\rho_v \vec{u}) + D_g\Delta\rho_v \tag{6}$$

where ε is the porosity of the TCES composite materials; ρ_v is the density of water vapor, kg•m^{-3}; $\vec{u}$ is the velocity vector, m•s^{-1}; D_g is the diffusion coefficient of water vapor in the reaction bed, m^2•s^{-1}; and S_w is the mass source and is expressed as:

$$S_w = zc_{s,i}\frac{\partial \alpha}{\partial t}M_v \tag{7}$$

where z is the stoichiometric number of the reaction; and M_v is the molecular mass of vapor, kg•mol^{-1}.

Furthermore, taking into account that the gas injected into the reactor consists of humidified airflow rather than solely water vapor, additional equations are of paramount importance to accurately describe the mass balance of the humidified airflow. The formulation of this equation is as follows:

$$\varepsilon\frac{\partial\rho_a}{\partial t}=S_w-\nabla(\rho_a\vec{u}) \tag{8}$$

where ρ_a is the density of the airflow, kg•m^{-3}.

3.3. Mass transport

The moist air mixture flow through the reaction bed is described by the Brinkman-Forchheimer extended Darcy model, the equation governing mass transport in this model can be expressed as follows [38]:

$$\frac{\rho_a}{\varepsilon}\frac{\partial\vec{u}}{\partial t}+\frac{\rho_a\vec{u}\nabla\vec{u}}{\varepsilon^2}=\nabla\left[-\vec{p}_a\mathrm{I}+\frac{\mu}{\varepsilon}(\nabla\vec{u}+(\nabla\vec{u})^T-\frac{2\mu}{3\varepsilon}(\nabla\vec{u})\mathrm{I})\right]+S_w\frac{\vec{u}}{\varepsilon^2}-\frac{\mu}{k}\vec{u} \tag{9}$$

where k is the permeability of the TCES composite materials in the reaction bed, m^2; and μ is the dynamic viscosity of the moist air mixture, Pa•s.

3.4. Energy conservation

The energy balance equation of the reaction bed in TCES system can be expressed as follows [35]:

$$(1-\varepsilon)\rho_s C_s\frac{\partial T}{\partial t}=\nabla(\lambda_{eff}\nabla T)-C_a\rho_a\vec{u}\nabla T+\dot{q} \tag{10}$$

where ρ_s is the density of the salt, kg•m^{-3}; C_s and C_a are the specific heat of the salt and air, J•kg^{-1}•K^{-1}; λ_{eff} is the effective thermal conductivity of the reaction bed, W•m^{-1}•K^{-1}; and $\dot{q}$ is the heat absorbed or released by the salt hydrate in the charging or discharging process, W•m^{-3}.

The effective thermal conductivity of the reaction bed can be described as follows:

$$\lambda_{eff}=(1-\varepsilon)\lambda_s+\varepsilon\lambda_m \tag{11}$$

where λ_s and λ_m represent the thermal conductivities of the solid salt and moist air mixture, respectively, W•m^{-1}•K^{-1}.

In the context of the charging or discharging processes, the heat released from or absorbed by the thermochemical reactions of TCES materials can be characterized as follows:

$$\dot{q}=-zc_{s,i}\frac{\partial\alpha}{\partial t}\Delta H_r \tag{12}$$

3.5. Boundaries and initial conditions

Considering that the TCES reactor is usually situated in an indoor environment with negligible local wind speeds, natural convection becomes the dominant heat transfer mechanism between the reactor and its surroundings. Therefore, the heat balance equation for the boundary of the TCES reactor can be represented as follows:

$$-\mathbf{n}(\lambda_{ins}\nabla T)=h_{ins}(T_{amb}-T) \tag{13}$$

where λ_{ins} is the thermal conductivity of the insulating material, W•m^{-1}•K^{-1}; h_{ins} is the natural convective heat transfer coefficient between the reactor and ambient air, W•m^{-2}•K^{-1}; and T_{amb} is the ambient air temperature, K.

At the initial stage, the temperature, pressure, conversion degree, and vapor concentration at any position within the TCES reactor are assumed to be uniformly distributed. The initial temperature of all components inside the TCES reactor is 20 °C, and the initial pressure within the reactor is at standard atmospheric pressure. Since this case study focuses on the discharge process, the initial conversion degree is set to 1.

The air variables remain constant at the reactor inlet. Non-slip boundary conditions are applied to the reactor walls. Since the TCES system is an open system, the operation pressure inside the reactor is equal to the ambient pressure p_{ref}. The temperature gradient at the reactor outlet is assumed to be zero. Additionally, the mass flow through the outlet boundary is predominantly convective, and any mass flow resulting from diffusion at this boundary is considered negligible.

Table 1
Key parameters of the tubular-type modular TCES reactor.

Parameters	Description	Value
M_v	Molecular mass of vapor (g·mol^{-1})	18.02
M_s	Molecular mass of salt (g·mol^{-1})	219.08
$c_{s,i}$	Molar concentration (mol·m^{-3})	1660
k	Permeability of TCES composite materials (m^2)	8.24·10^{-6}
C_s	Specific heat of the salt (J·kg^{-1}·K^{-1})	0.626
λ_s	Thermal conductivity of the salt (W·m^{-1}•K^{-1})	0.0669
E	Porosity	0.64
E_a	Activation energy (kJ·mol^{-1})	44.7 [43]
ΔH_r	Reaction enthalpy (kJ•mol^{-1})	53.4 [44]
ΔS_r	Reaction entropy (J·mol^{-1} K^{-1})	104.62 [45]
D_g	Gas diffusion coefficient (m^2·s^{-1})	2.3·10^{-8}
C_a	Specific heat of the airflow (J·kg^{-1}·K^{-1})	1005
R	Universal gas constant (J·mol^{-1}·K^{-1})	8.314
P_{ref}	Reference pressure (Pa)	101325
L	Length of the reactor (m)	0.4
W	Width of the reactor (m)	0.4
H	Height of the reactor (m)	0.4
l_{out}	Length of the outer perforated pipe (m)	0.4
l_{in}	Length of the inner perforated pipe (m)	0.0385
Φ_{out}	Diameter of the outer perforated pipe (m)	0.05
Φ_{in}	Diameter of the inner perforated pipe (m)	0.02

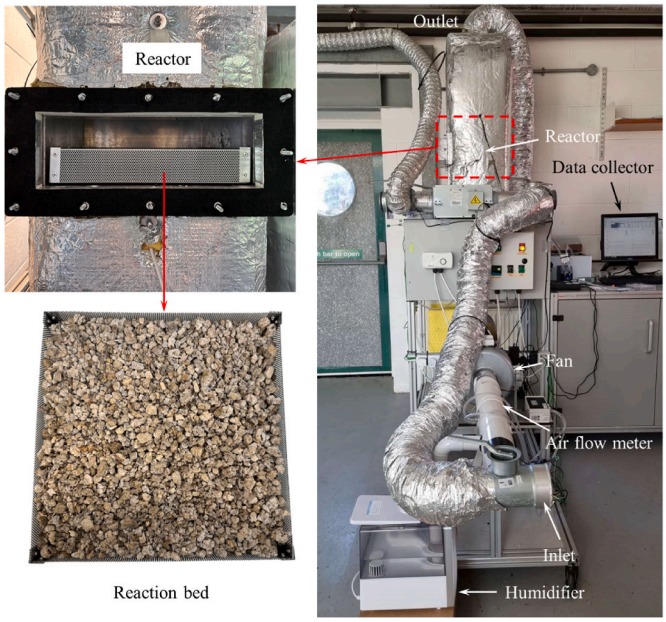

Fig. 5. Photos of a versatile lab-scale TCES system and internal view of the reactor.

3.6. Performance evaluation metrics

In this study, the TCES system's equivalent thermal efficiency during the discharging process is defined as the ratio of the heat absorbed by the airflow to the sum of the heat released by the TCES composite materials and the equivalent heat converted from the fan power consumption (Abbreviated as "Fan energy consumption" in Figure and Table). This definition can be expressed mathematically as follows:

$$\eta_{th}=\frac{Q_{ab}}{Q_{re}+Q_{fan}} \tag{14}$$

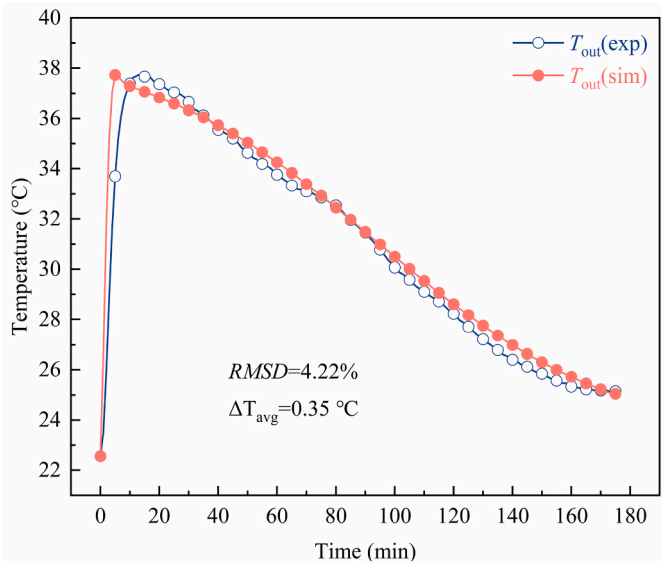

Fig. 6. Simulation and experiment results of the reactor outlet airflow temperature.

where Q_{ab} is the heat absorbed by the airflow, kJ; and Q_{re} is the amount of heat released from the TCES composite materials, kJ; and Q_{fan} is the heat consumed by the duct fan, kJ.

The amount of heat absorbed by the airflow is given as:

$$Q_{ab,a} = \int P_{out} dt = \int \dot{m}_a C_a \left(T_{a,out} - T_{a,in}\right) dt \tag{15}$$

where P_{out} is the output power of the TCES system, W; $\dot{m}_a$ is the mass flow rate of the airflow, kg·s^{-1}; $T_{a,out}$ and $T_{a,in}$ are the airflow temperatures at the inlet and outlet of the reactor, respectively, K.

The amount of heat released from thermochemical reaction of the TCES materials is given as:

$$Q_{re} = \int\int z c_{s,i} \frac{\partial \alpha}{\partial t} \Delta H_t dt dV \tag{16}$$

The equivalent heat converted from the fan power consumption is represented by:

$$Q_{fan} = \frac{\int E_{fan} dt}{\eta_T} = \frac{\int (\Delta p \dot{V}_a) dt}{\eta_T \eta_{fan}} \tag{17}$$

where E_{fan} is the power of the duct fan, W; η_T is the conversion efficiency of the thermal power plant and is set to 49.9 % in this study [41]. Δp is the differential pressure between the TCES system inlet and outlet, Pa; $\dot{V}_a$ is the volume flow rate of air, m^3•s^{-1}; and η_{fan} is the fan efficiency, % [42].

3. Model validation

In this numerical study, the transient solver within COMSOL Multiphysics was employed to simulate multiple physical phenomena within the thermal-chemical reactor. Equations ((3), (7), (10) and (11) were employed to model the processes of thermochemical reactions, mass transfer, momentum transfer, and heat transfer within the reactor. The simulation was performed with a time step of 1 s and a fine grid consisting of 1,962,618 elements. The Backward Differentiation Formula (BDF) method was chosen for time stepping and the Generalized Minimal Residual Method (GMRES) was used as the iterative solver. Residual values were set to 10^{-6} to ensure numerical stability and convergence of the simulation results. The details of the key simulation parameters are presented in Table 1.

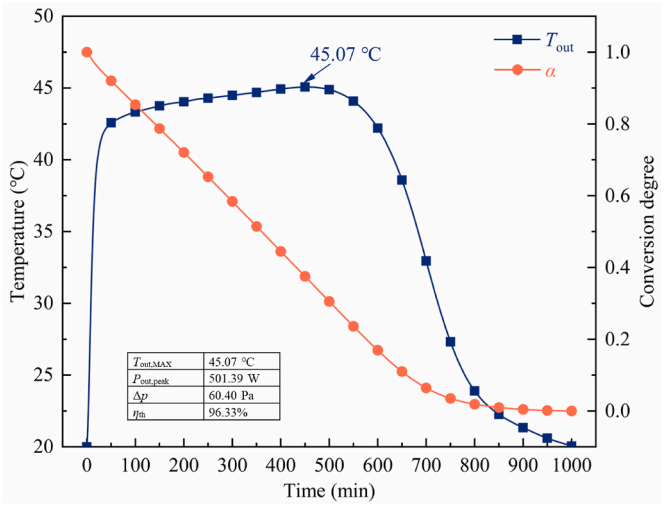

Fig. 7. Conversion degree of salt hydrates and the outlet airflow temperature of the tubular-type modular TCES reactor.

In order to validate the mathematical model proposed in this study, a versatile laboratory-scale TCES test rig was constructed and subjected to experimental analysis, as depicted in Fig. 5. This TCES system comprises several components, with the primary unit consisting of a reactor housing a metal mesh-packed bed filled with TCES composite materials positioned at its centre. In operation, the ambient airflow is firstly humidified using a humidifier. Subsequently, the humidified airflow passes through the packed bed, where it is heated. Finally, the heated airflow is exhausted from the TCES system.

To facilitate a comparison between the simulated results and experimental measurements, the root mean square deviation (*RMSD*) is employed as a quantitative metric, as defined by the following equation [46]:

$$RMSD = \sqrt{\frac{\sum \left[\left(x_{sim,i} - x_{exp,i}\right)/x_{exp,i}\right]^2}{n}} \tag{18}$$

The simulation and experimental results of the reactor outlet airflow temperature are presented in Fig. 6. The simulated and experimental outlet airflow temperatures show a rapid increase during the initial stage, reaching peaks of 37.73 °C and 37.72 °C, respectively. Subsequently, both temperature curves decline steadily until the end of the discharging process. Throughout the entire discharge process, the average temperature difference between the simulated and experimental outlet airflow temperatures is 0.36 °C. The *RMSD* value of the outlet air temperature is calculated to be 4.22 % using Eq. (18). The comparison demonstrates a good agreement between the simulation results obtained using the proposed mathematical model and the experimental data. Thus, the mathematical model developed in Section 3 accurately predicts the performance of the proposed tubular-type modular TCES reactor during the discharging process.

5. Results and discussion

Numerical analysis was performed to assess the thermal performance of the tubular-type modular TCES reactor during the discharge process, based on the mathematical model established in Section 3. A comparative study was also conducted with the plate-type modular TCES reactor.

5.1. Performance during whole discharging process

The thermal performance of the tubular-type modular TCES reactor during the complete discharging process is investigated in this section. While lower reactor inlet temperatures can provide a more accurate

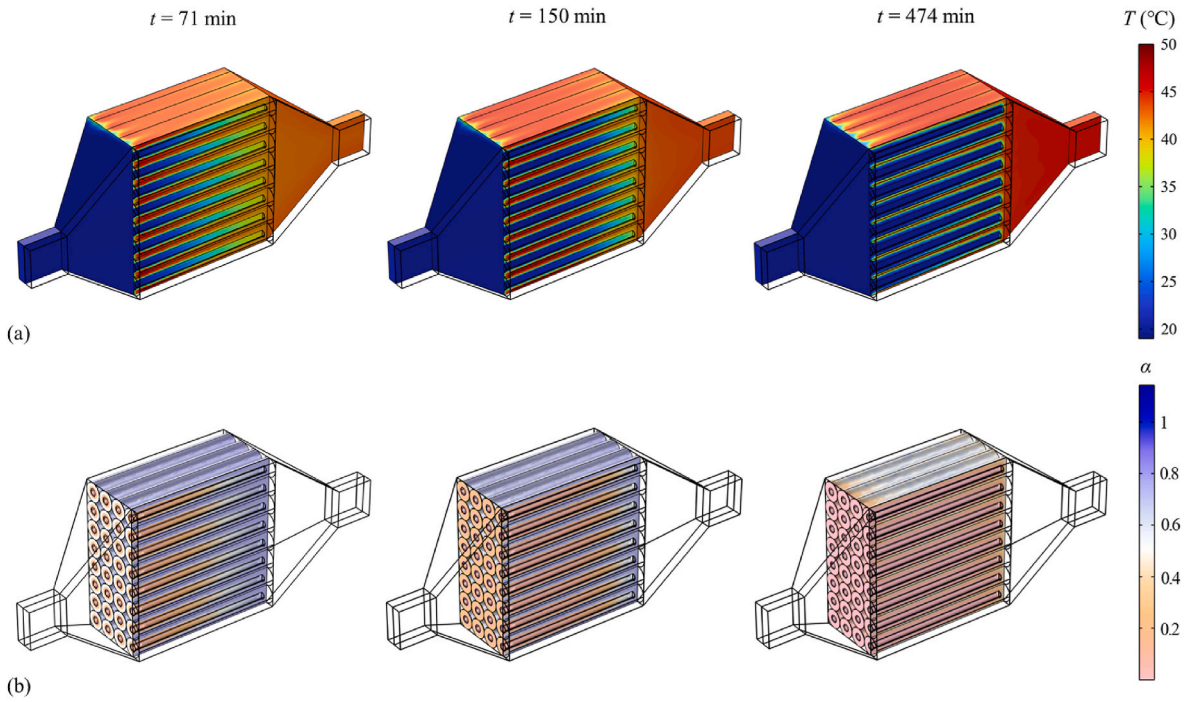

Fig. 8. (a)Temperature and (b) conversion degree distributions of the tubular-type reactor at 71st minute, 150th minute and 474th minute, respectively.

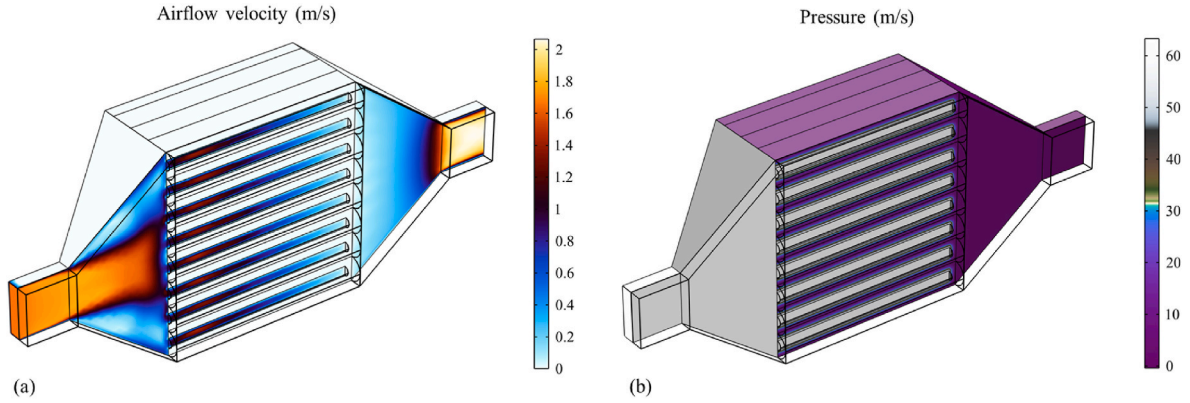

Fig. 9. Distribution of air flow velocity and pressure within the reactor upon the attainment of a steady-state condition for the airflow.

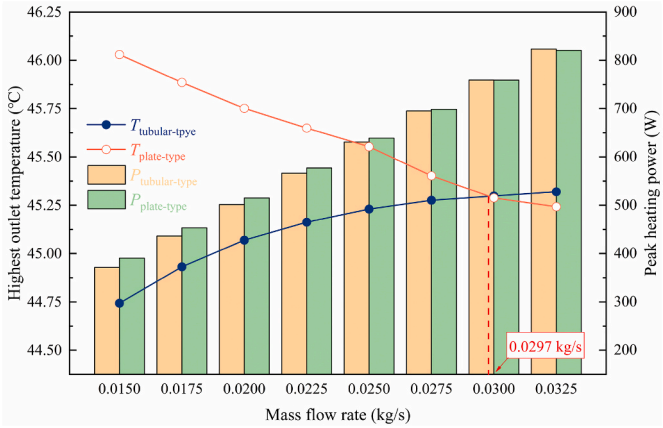

Fig. 10. Compare the highest outlet airflow temperature and peak heating power of the tubular-type and plate-type modular reactors under various inlet air mass flow rate conditions.

assessment of the TCES system's performance in winter conditions and predict its capability in practical applications, other factors need to be taken into consideration when selecting the inlet air temperature. Lower temperatures may result in slower reaction rates or lower energy release rates due to the low moisture saturation of cold air, thereby affecting the performance and efficiency of the TCES system. Directly introducing cold air into the reactor is not recommended; instead, preheating the air and ensuring its ability to carry more moisture before entering the reactor is necessary. In this study, it is assumed that the airflow has been preheated and humidified to 20 °C and 86 % relative humidity before entering the reactor. The mass flow rate of the inlet airflow is set to 0.02 kg/s.

Fig. 7 depicts the conversion degree of salt hydrates along with the outlet airflow temperature of the tubular-type modular TCES reactor. Initially, the conversion degree experiences a rapid decrease from 1, which can be attributed to the entry of moist air into the reactor, causing the dehydrated salt to absorb moisture and transform into salt hydrates. Simultaneously, the outlet airflow temperature of the reactor shows a sudden increase in the early stages, followed by a sluggish rise after 37th minute until it reaches a peak of 45.07 °C at

474th minute. This distinctive trend in the outlet airflow temperature can be attributed to the process of moisture absorption and conversion of dehydrated salt into salt hydrates, which releases heat. Additionally, the high conversion rate of dehydrated salts to salt hydrates during the initial stage contributes to the temperature radically rising from 0 to 71st minutes. Fig. 8 illustrates the distribution of temperature and conversion degree within the tubular modular reactor (including the central cross-section of the fifth row of tubular reaction beds) at the 71st, 150th, and 474th minutes. Concurrently, Fig. 9 portrays the distribution of air flow velocity and pressure within the reactor upon the attainment of a steady-state condition for the airflow.

Subsequently, as the moisture content in the salt hydrate increases, the conversion rate of dehydrated salts to salt hydrates decelerates. Consequently, the outlet airflow temperature of the reactor decreases in tandem until the conversion degree reaches zero. At this point, the reactor outlet airflow temperature becomes equal to the inlet airflow temperature, signifying the completion of the discharging process. Throughout the discharging process, the tubular-type modular TCES reactor achieves a peak output power of 501.39 W, and the pressure drop between the inlet and outlet of the reactor measures 60.40 Pa. Remarkably, the equivalent thermal efficiency is an impressive 96.33 %.

5.2. Performance comparison between tubular-type and plate-type modular reactors under different inlet mass flow rates

This section presents a performance comparison between the tubular-type and plate-type modular reactors under different air mass flow rates. The structure of the plate-type modular reactor is as previously described in the literature, and the same TCES composite material (e.g., vermiculite-$CaCl_2$) was used. Furthermore, the mass of TCES composite materials in both reactors is ensured to be consistent. In this section, the only varying parameter is the inlet air mass flow rate, while all other inlet and boundary conditions were kept unchanged as detailed in Section 5.1.

Fig. 10 illustrates the highest outlet airflow temperature and reactor peak heating power of the tubular-type and plate-type modular reactors under various inlet air mass flow rate conditions. When the inlet air mass flow rate is 0.015 kg/s, the highest outlet airflow temperature of the tubular-type modular reactor is lower than that of the plate-type modular reactor, measuring 44.74 °C and 46.03 °C, respectively. As the inlet air mass flow rate increases, the highest outlet airflow temperature of the plate-type modular reactor exhibits a decreasing trend, while an opposite trend is observed for the tubular-type modular reactor. This phenomenon can be attributed to the increase in longitudinal airflow velocity within the reaction bed as the inlet air mass flow rate of the reactor rises. On one hand, the increased longitudinal airflow velocity facilitates a faster passage of airflow through the reaction bed, leading to a reduced heat transfer time between the airflow and the TCES composite materials, thus lowering the outlet airflow temperature of the reactor. On the other hand, the increased longitudinal airflow velocity within the reaction bed promotes a higher hydration rate of the dehydrated salts, resulting in an increased heat release rate from the TCES composite materials, as described by Eq. (12). When the longitudinal airflow velocity within the reaction bed is relatively low, the heat release rate of the TCES composite materials has a more pronounced impact, leading to an increase in the outlet temperature as the longitudinal airflow velocities within the reaction bed increase. However, at higher longitudinal airflow velocities within the reaction bed, the effect of reduced heat transfer time prevails over the increased heat release rate, causing a decrease in the outlet temperature as the longitudinal airflow velocities within the reaction bed increase. While both reactor types exhibit the same inlet air mass flow rate, the plate-type modular reactor shows an approximately 23 % increase in longitudinal airflow velocity within the reaction bed when compared to the tubular-type modular reactor. Consequently, within this range of inlet air mass flow rates, the highest outlet airflow temperature of the plate-type modular reactor exhibits a decreasing trend with increasing inlet air mass flow rate, whereas the tubular-type modular reactor shows an opposite trend. At an inlet air mass flow rate of 0.0297 kg/s, both module reactors display the same highest outlet airflow temperature. However, as the inlet air mass flow rate continues to increase, the highest airflow temperature of the tubular-type modular reactor surpasses that of the plate-type modular reactor. At an inlet air mass flow rate of 0.0325 kg/s, the highest outlet airflow temperatures in the tubular-type and plate-type modular reactors are measured at 45.32 °C and 45.24 °C, respectively.

Similar to the highest outlet airflow temperature of the reactor, when the inlet air mass flow rate is 0.015 kg/s, the tubular-type modular reactor's peak heating power is lower than that of the plate-type modular reactor, measuring 371.15 W and 390.45 W, respectively. The peak heating power of both types of modular reactors increases with an increase in the inlet airflow mass flow rate. This is due to the enhanced longitudinal airflow within the reaction bed, which leads to an increase in the hydration rate of the dehydrated salts and, consequently, an elevated heat release rate from the TCES composite materials. Furthermore, the increase in longitudinal airflow also augments the convective heat transfer between the airflow and the TCES composite materials, resulting in more heat being transferred from the TCES composite materials to the airflow. The peak heating power of the tubular-type

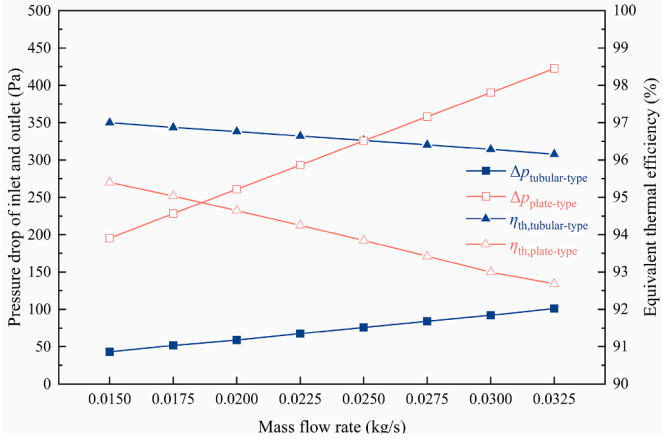

Fig. 11. Results of pressure drops and system equivalent thermal efficiency of the tubular-type and plate-type modular reactors under different inlet air mass flow rates.

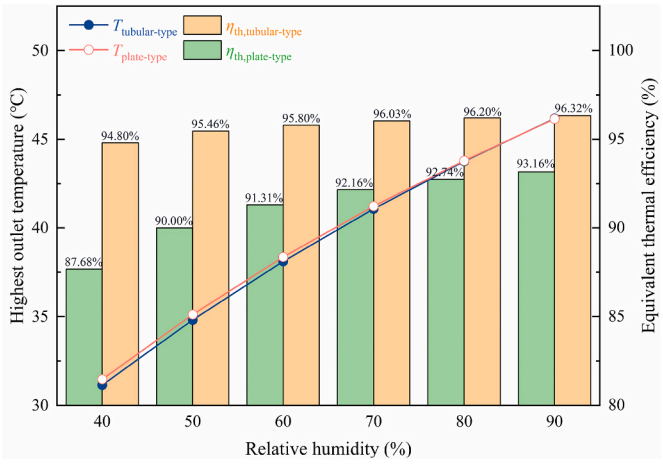

Fig. 12. Influence of inlet air relative humidity on the highest outlet airflow temperature and equivalent thermal efficiency of both reactors.

Table 2
Influence of inlet air relative humidity on discharging time, pressure drops, and equivalent heat converted from the fan power consumption of both reactors.

Relative humidity (%)	Discharging time (min)		Pressure drops (Pa)		Fan energy consumption (kJ)	
	$t_{tubular\text{-}type}$	$t_{plate\text{-}type}$	$\Delta p_{tubular\text{-}type}$	$\Delta p_{plate\text{-}type}$	$Q_{fan,\ tubular\text{-}type}$	$Q_{fan,\ plate\text{-}type}$
90	698	721	92.72	390.41	277.68	948.62
80	758	763	92.66	390.13	304.40	1038.31
70	836	824	92.60	389.79	339.84	1160.48
60	945	916	92.53	389.38	390.48	1341.56
50	1123	1096	92.46	388.91	462.74	1617.63
40	1503	1443	92.36	388.34	602.20	2110.27

modular reactor surpasses that of the plate-type modular reactor when the inlet air mass flow rate exceeds 0.0297 kg/s and continues to increase.

Fig. 11 illustrates the pressure drop and the system equivalent thermal efficiency of the tubular-type and plate-type modular reactors under different inlet air mass flow rates. Both tubular-type and plate-type modular reactors experience an increase in the pressure drop as the inlet air mass flow rate increases. However, the plate-type modular reactor exhibits significantly higher pressure drops compared to the tubular-type modular reactor, and this difference escalates with an increase in the inlet air mass flow rate. Specifically, when the air mass flow rate is 0.015 kg/s, the pressure drop for the tubular-type and plate-type modular reactors are 43.12 Pa and 195.25 Pa, respectively. The pressure drop in the plate-type modular reactor is approximately 5 times that of the tubular-type reactor. When the air mass flow rate is 0.0325 kg/s, the pressure drop for the tubular-type and plate-type modular reactors are 101.19 Pa and 422.54 Pa, respectively. The pressure drop in the plate-type modular reactor is approximately 4 times that of the tubular-type reactor.

Due to the maintained low levels of pressure drop in the tubular-type modular reactor, the equivalent thermal efficiency experiences a slow decrease with the increase in air mass flow rate, yet it remains above 95 %. In contrast, the significant rise in pressure drops within the plate-type modular reactor results in a substantial increase in the equivalent thermal efficiency of the plate-type modular reactor with the augmentation of inlet air mass flow rate, demonstrating a comparatively lower equivalent thermal efficiency. At an air mass flow rate of 0.015 kg/s, the comprehensive thermal efficiency of the plate-type modular reactor stands at 95.40 %, differing by approximately 7% points from the tubular-type configuration. With the escalation of inlet air mass flow rate, this efficiency further declines. When the air mass flow rate reaches 0.0325 kg/s, the efficiency drops to 92.68 % for the plate-type modular reactor, diverging by approximately 4% points from the tubular-type counterpart.

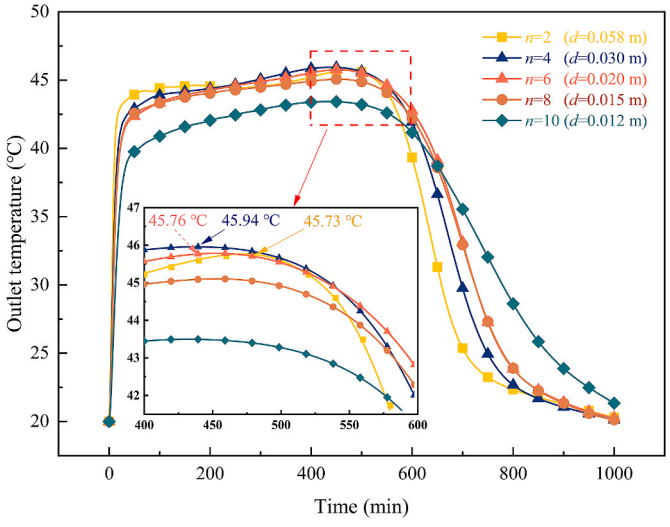

Fig. 13. Effect of the number of rows and columns on the reactor outlet airflow temperature.

5.3. *Performance comparison between tubular-type and plate-type modular reactors under different inlet relative humidity conditions*

This section compares the performance of tubular-type and plate-type modular reactors under different inlet air relative humidity conditions. Fig. 12 illustrates the influence of inlet air relative humidity on the highest outlet airflow temperature of both types of reactors. The highest outlet airflow temperature in both tubular-type and plate-type modular reactors increases as the inlet air relative humidity of the reactor rises. This is attributed to the accelerated hydration rate of dehydrated salts as the inlet air relative humidity increases, resulting in a higher heat release rate as described by Eq (12). Specifically, at an inlet air relative humidity of 40 %, the highest outlet airflow temperatures for the tubular-type and plate-type modular reactors are 31.15 °C and 31.47 °C, respectively. As the inlet air relative humidity continues to increase, the highest outlet airflow temperature in both tubular-type and plate-type modular reactors constantly rises, reaching 45.28 °C at an inlet air relative humidity of 83 % at the same time. Subsequently, with a further increase in the inlet air relative humidity of the reactor, the highest outlet airflow temperature of the tubular-type modular reactor surpasses that of the plate-type modular reactor. At the inlet air relative humidity of 90 %, the highest outlet airflow temperatures for the tubular-type and plate-type modular reactors are 46.17 °C and 46.15 °C, respectively.

As indicated in Table 2, both the pressure drop of both tubular-type and plate-type modular reactors do not show a significant increase with higher relative humidity of the inlet air. They remain within the range of 92.36–92.72 Pa and 388.34–391.41 Pa, respectively. However, the discharging duration of both reactors significantly decreases as the relative humidity of the inlet air increases. This reduction is attributed to the enhanced salt dehydration rate in higher humidity conditions. At an inlet air relative humidity of 90 %, the discharge durations for the tubular-type and plate-type reactors are 698 min and 721 min, respectively. These durations are nearly half of the discharge durations observed at an inlet air relative humidity of 40 %. Due to the consistent pressure drop levels and reduced reactor discharging time, the equivalent heat converted from the fan power consumption also decreases with higher inlet air humidity. When the inlet air relative humidity is 90 %,

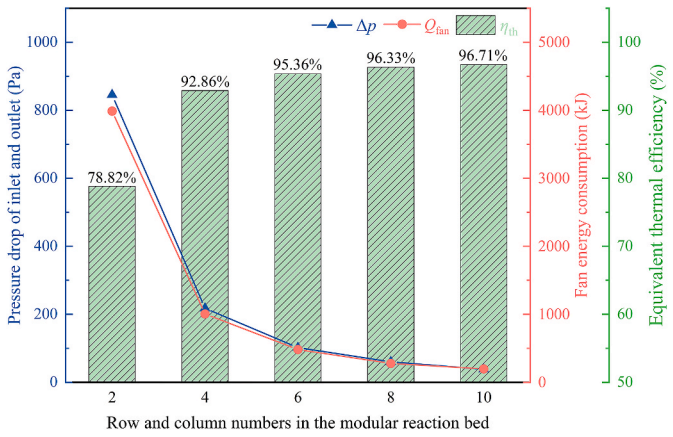

Fig. 14. Effect of the number of rows and columns on the reactor's pressure drop, equivalent heat converted from the fan power consumption, and equivalent thermal efficiency.

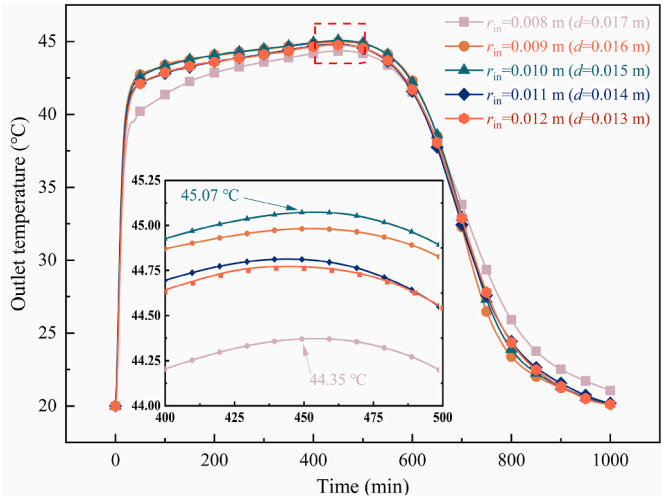

Fig. 15. Variation in outlet airflow temperature of the reactor for different radii of inner perforated pipe.

the equivalent heat converted from the fan power consumption for both the tubular-type and plate-type reactors is about half of that at 40 %. This decrease in equivalent heat converted from the fan power consumption leads to an increase in the equivalent thermal efficiency of both reactor types with rising inlet air relative humidity, as depicted in Fig. 12. The equivalent thermal efficiency of the tubular-type modular reactor slightly increases with higher relative humidity. With an increase in inlet air relative humidity from 40 % to 90 %, the equivalent thermal efficiency of the tubular-type modular reactor rises from 94.80 % to 96.32 %. In contrast, the equivalent thermal efficiency of the plate-type modular reactor demonstrates a more pronounced increase with higher relative humidity, closing the gap with the tubular-type reactor. As the inlet air relative humidity increases from 40 % to 90 %, the equivalent thermal efficiency of the plate-type modular reactor increases significantly, from 87.68 % to 93.16 %, marking a gain of nearly 5% points. Despite this gain, the difference from the tubular-type modular reactor remains approximately 3% points.

5.3. Effect of row and column numbers in the modular reaction bed matrix

Due to the equal width and height of the tubular-type modular reactor, the tubular-type modular reaction bed placed inside can be considered as a square matrix, where the number of rows and columns is represented by n. In this model, a symmetric structure is adopted in the simulation, so only even values of n are chosen. The inlet and boundary conditions are the same as in Section 5.1. The influence of n on the highest outlet airflow temperature of the reactor is shown in Fig. 13. As n increases from 2 to 4 (corresponding to a decrease in the thickness d of the modular bed from 0.058 m to 0.03 m), the highest outlet air temperature of the reactor rises from 45.73 °C to 45.94 °C. With further increments in n, the highest outlet air temperature of the reactor consistently decreases. When n = 10 (i.e., d = 0.012 m), the highest outlet air temperature of the reactor drops to 43.43 °C.

The impact of n on the pressure drop of the reactor, the equivalent heat converted from the fan power consumption, and the equivalent thermal efficiency are illustrated in Fig. 14. As n increases from 2 to 4, the pressure drop decreases significantly from 845.53 Pa to 217.85 Pa. With further increments in n, the pressure drop reduction slows down. At n=10, the pressure drop diminishes to 38 Pa, which is one-twentieth of the value at n=2. This reduction occurs due to the decreased spacing between the outer perforated pipe and inner perforated pipe within the tubular-type module, resulting in a shorter airflow path through the reactor bed.

The trend in the variation of the equivalent heat converted from the fan power consumption mirrors that of the pressure drop, though with a slightly smaller reduction. This is attributed to the fact that as the value of n increases, the duration of reactor discharge also increases. However, the equivalent thermal efficiency behaves inversely to the trends of pressure drop and the equivalent heat converted from the fan power consumption. As n increases from 2 to 4, the equivalent heat converted from the fan power consumption surges significantly from 78.82 % to 92.86 %. Subsequently, as n continues to increase, this value growth slows down. Upon reaching n equals 10, the equivalent thermal efficiency escalates to 96.61 %. This is due to the reduction in the equivalent heat converted from the fan power consumption with increasing values of n.

5.5. Effect of inner perforated pipe radius

In this section, we investigate the impact of the inner perforated pipe radius (i.e., r_{inner}) on the discharging performance of the tubular-type modular reactor while keeping the TCES composite material volume and the inlet condition unchanged. The influence of different inner perforated pipe radii on the outlet airflow temperature of the reactor is shown in Fig. 15. The temperature curves corresponding to five r_{inner} values all exhibited a sharp increase in the initial stage, followed by a slow increase, reaching their peak at the 450th minute. As r_{inner} increased from 0.008 m (i.e., d = 0.017 m), the highest outlet airflow temperature of the reactor continued to rise until r_{inner} reached 0.01 m (i.e., d = 0.015 m), where the highest outlet airflow temperature reached its maximum value of 45.07 °C. With further increases in r_{inner}, the highest outlet airflow temperature of the reactor began to decrease. When r_{inner} was 0.012 m (i.e., d = 0.013 m), the highest outlet airflow temperature dropped to 44.76 °C. Notably, the highest outlet temperature values for the five different inner perforated pipe radii were similar. Among them, the lowest highest outlet temperature was observed at r_{inner} = 0.008 m, which was only 0.98 °C lower than r_{inner} = 0.01 m. As time progressed, all five temperature curves started to decrease until the hydration reaction was complete.

The impact of the internal perforated pipe radius on the reactor's pressure drop, the equivalent heat converted from the fan power consumption, and equivalent thermal efficiency is shown in Fig. 16. The reactor's pressure drop decreases as r_{inner} increases, decreasing from 84.21 Pa (r_{inner} = 0.008 m) to 42.83 Pa (r_{in} = 0.012 m), which is nearly half of the original value. This is because the outer perforated pipe radius remains fixed, as r_{inner} increases, the spacing between the outer and inner perforated pipes in the tubular-type modular reaction bed becomes smaller, resulting in shorter airflow paths through the reaction

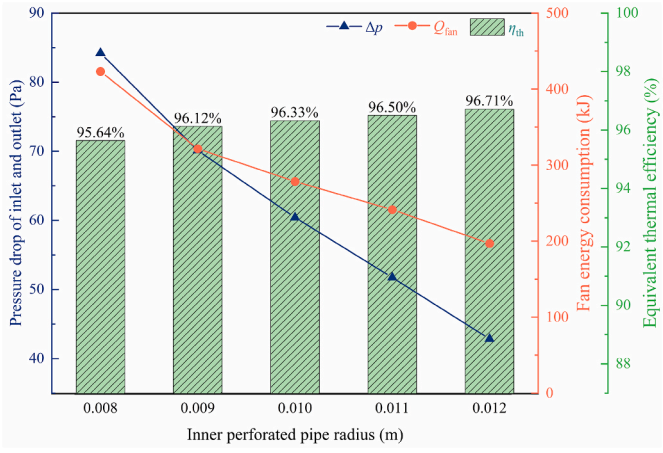

Fig. 16. Effect of the inner perforated pipe radius on the reactor's pressure drop, equivalent heat converted from the fan power consumption, and equivalent thermal efficiency.

bed. Moreover, the equivalent heat converted from the fan power consumption also decreases with an increase in r_{inner} due to the reduced pressure drop. When r_{inner} is 0.008 m, the equivalent heat converted from the fan power consumption is 423.17 kJ, and when r_{inner} increases to 0.012 m, the equivalent heat converted from the fan power consumption decreases by more than half, reaching 196.80 kJ. However, the equivalent thermal efficiency does not exhibit significant changes with an increase in r_{inner}, remaining consistently above 95 %. This is attributed to the relatively small values of equivalent heat converted from the fan power consumption, which cannot exert a substantial influence on the equivalent thermal efficiency.

6. Conclusion

In this study, a novel tubular-type modular TCES reactor was proposed and a mathematical model was established using COMSOL software. A Comprehensive numerical study was implemented to assess the performance of the proposed reactor with comparison with a plate-type modular reactor under different inlet conditions and evaluate the impacts of different structural parameters on reactor performance. The simulation results led to the following conclusions.

(1) To validate mathematical model, a laboratory-scale TCES system was built. The simulated and experimental results agree well, with a minor average temperature difference of the outlet airflow temperature (e.g., 0.36 °C), and an RMSD of 4.22 %.The outlet airflow temperature of the reactor rapidly increases after the humid air enters the reactor and reaches its peak at 45.07 °C at the 474th minute. The reactor achieves a peak output power of 501.39 W, with a pressure drop of 60.40 Pa, and an impressive equivalent thermal efficiency of 96.33 %.

(2) Under identical inlet conditions, the difference in peak outlet air temperatures between tubular-type and plate-type modular reactors is minimal. As the relative humidity of the inlet airflow rises, their maximum temperature lift increases. For instance, at a relative humidity of 90 %, the maximum temperature lift is nearly 15 °C higher compared to a relative humidity of 40 %. Plate-type modular reactors exhibit approximately 4–5 times the pressure drop when compared to tubular-type modular reactors. This discrepancy can be attributed to the greater thickness of plate-type modular reaction beds relative to tubular ones. Under the same inlet conditions, plate-type modular reactors demonstrate a lower equivalent thermal efficiency than tubular-type modular reactors, with the primary factor being the pressure drop. Furthermore, with an increase in the inlet air mass flow rate, the equivalent thermal efficiency of both reactor types decreases, while at the same time, the gap in their effective thermal efficiencies widens. However, it's worth noting that the effective efficiency of both reactor types increases as the inlet air relative humidity rises, and simultaneously, the difference in their effective thermal efficiencies decreases.

(3) The structural parameters of tubular-type modular reactors, including matrix row and column count (n) and the inner perforated tube radius (r_{inner}), exert a modest impact on maximum temperature lift, assuming the TCES composite material volume remains constant. Notably, as both n and r_{inner} increase, there are a reduction in pressure drop and an improvement in equivalent thermal efficiency, primarily attributed to decreased bed thickness. The influence of n is particularly pronounced in comparison to r_{inner}. For example, with r_{inner} fixed at the base case of 0.01 m, the pressure drop at $n = 10$ (i.e., $d = 0.012$ m) is merely 38 Pa, whereas at $n = 2$ (i.e., $d = 0.058$ m), it surges to nearly 25 times that value. As n progressively rises, equivalent thermal efficiency sees a substantial increase. When n reaches 10, equivalent thermal efficiency soars to 96.61 %, marking an improvement of nearly 18% points over the performance at $n = 2$.

While both reactor types exhibit similar maximum temperature lift, tubular structures offer better axial flexural strength compared to plate structures. This makes tubular modular beds used in transverse reactor configurations more accessible for processing. Additionally, the tubular structure allows for better dispersion of TCES composite materials, leading to a reduction in bed thickness for each modular reactor bed, thus decreasing pressure drop and increasing equivalent thermal efficiency. However, it is important to note that although increasing the number of modular reactor beds and the inner tube radius can improve the equivalent thermal efficiency. In practical design, a balance must be struck between equivalent thermal efficiency and the stacking of TCES composite materials, as excessively thin stack thickness can significantly reduce stacking density. An experimental-scale reactor will be designed in the near future to assess its real-world performance.

CRediT authorship contribution statement

Yong Zhang: Software, Formal analysis, Investigation, Writing – original draft, Writing – review & editing. **Mingke Hu:** Conceptualization, Supervision, Methodology, Formal analysis, Investigation, Writing – review & editing. **Ziwei Chen:** Formal analysis, Writing – review & editing. **Yuehong Su:** Conceptualization, Supervision, Project administration, Funding acquisition, Writing – review & editing. **Saffa Riffat:** Resources, Project administration, Writing – review & editing.

Declaration of competing interest

The authors declare that they have no known competing financial interests or personal relationships that could have appeared to influence the work reported in this paper.

Acknowledgements

The authors would like to acknowledge the Engineering and Physical Sciences Research Council (grant number: EP/T021233/1) for the financial support to this research.

Nomenclature

A_{freq}	Pre-exponential Arrhenius factor, s^{-1}
C	Specific heat, J•kg^{-1}•K^{-1}
c	Mole concentration, mol•m^{-3}
D_g	Gas diffusivity in reactive bed, m^2•s^{-1}
d	Reaction bed thickness
E_a	Arrhenius activation energy, J•mol^{-1}
H	Enthalpy, kJ
k	Permeability of TCES composite material, m^2
L	Length of reactor, m

l	Length of perforated pipe, m
M	Molecular mass, g•mol^{-1}
$\dot{m}$	Mass flow rate, kg•s^{-1}
P	Power, W
p	Pressure, Pa
$\dot{q}$	Volume power source, W•m^{-3}
Q	Thermal energy, J
R	Ideal gas constant, J•mol^{-1}•K^{-1}
r	Radius, m
R_{kin}	Kinetic factor, s^{-1}
S	Entropy, J•mol^{-1}•K^{-1}
S_w	Mass source of water vapor, kg•m^{-3}·s^{-1}
T	Temperature, K or °C
t	Time, min
$\overrightarrow{u}$	Velocity vector, m•s^{-1}
V	Volume
$\dot{V}_a$	Volume flow rate, m^3·s^{-1}
z	Stoichiometric number

Greek symbols

ρ	Density, kg•m^{-3}
ε	porosity
α	Reaction conversion degree
η	Equivalent thermal efficiency, %
μ	Dynamic viscosity, Pa•s
λ	Thermal conductivity, W•m^{-1}•K^{-1}

Subscripts

a	Air
ab	Heat absorbed
amb	Ambient
dis	Discharging
eff	Effective
eq	Equilibrium state
f	Final
fan	Fan
i	Initial
in	Inlet
inner	Inner perforated pipe
ins	Insulation plate
kin	Kinetic
re	Heat release
out	Outlet
outer	Outer perforated pipe
v	Vapor

References

[1] National Energy Action (NEA) | Energy Crisis, (n.d.). https://www.nea.org.uk/energy-crisis/(accessed February 3, 2023).

[2] B. Michel, N. Mazet, S. Mauran, D. Stitou, J. Xu, Thermochemical process for seasonal storage of solar energy: characterization and modeling of a high density reactive bed, Energy 47 (2012) 553–563, https://doi.org/10.1016/J.ENERGY.2012.09.029.

[3] R. Han, S. Xing, X. Wu, C. Pang, S. Lu, Y. Su, Q. Liu, C. Song, J. Gao, Relevant influence of alkali carbonate doping on the thermochemical energy storage of Ca-based natural minerals during CaO/CaCO3 cycles, Renew. Energy 181 (2022) 267–277, https://doi.org/10.1016/J.RENENE.2021.09.021.

[4] A. Fopah Lele, F. Kuznik, O. Opel, W.K.L. Ruck, Performance analysis of a thermochemical based heat storage as an addition to cogeneration systems, Energy Convers. Manag. 106 (2015) 1327–1344, https://doi.org/10.1016/j.enconman.2015.10.068.

[5] A.I. Fernandez, M. Martnez, M. Segarra, I. Martorell, L.F. Cabeza, Selection of materials with potential in sensible thermal energy storage, Sol. Energy Mater. Sol. Cell. 94 (2010) 1723–1729, https://doi.org/10.1016/J.SOLMAT.2010.05.035.

[6] B. Zalba, J.M. Marín, L.F. Cabeza, H. Mehling, Review on thermal energy storage with phase change: materials, heat transfer analysis and applications, Appl. Therm. Eng. 23 (2003) 251–283, https://doi.org/10.1016/S1359-4311(02)00192-8.

[7] P. Tatsidjodoung, N. Le Pierrès, L. Luo, A review of potential materials for thermal energy storage in building applications, Renew. Sustain. Energy Rev. 18 (2013) 327–349, https://doi.org/10.1016/J.RSER.2012.10.025.

[8] D. Aydin, S.P. Casey, S. Riffat, The latest advancements on thermochemical heat storage systems, Renew. Sustain. Energy Rev. 41 (2015) 356–367, https://doi.org/10.1016/J.RSER.2014.08.054.

[9] K.E. N'Tsoukpoe, T. Schmidt, H.U. Rammelberg, B.A. Watts, W.K.L. Ruck, A systematic multi-step screening of numerous salt hydrates for low temperature thermochemical energy storage, Appl. Energy 124 (2014) 1–16, https://doi.org/10.1016/j.apenergy.2014.02.053.

[10] Q. Touloumet, L. Silvester, L. Bois, G. Postole, A. Auroux, Water sorption and heat storage in CaCl2 impregnated aluminium fumarate MOFs, Sol. Energy Mater. Sol. Cell. 231 (2021), 111332, https://doi.org/10.1016/J.SOLMAT.2021.111332.

[11] S. Wei, W. Zhou, R. Han, J. Gao, G. Zhao, Y. Qin, C. Wang, Influence of minerals with different porous structures on thermochemical heat storage performance of CaCl2-based composite sorbents, Sol. Energy Mater. Sol. Cell. 243 (2022), 111769, https://doi.org/10.1016/J.SOLMAT.2022.111769.

[12] S.P. Casey, D. Aydin, S. Riffat, J. Elvins, Salt impregnated desiccant matrices for "open" thermochemical energy storage - hygrothermal cyclic behaviour and energetic analysis by physical experimentation, Energy Build. 92 (2015) 128–139, https://doi.org/10.1016/j.enbuild.2015.01.048.

[13] T. Yan, C.Y. Wang, D. Li, Performance analysis of a solid-gas thermochemical composite sorption system for thermal energy storage and energy upgrade, Appl.

Therm. Eng. 150 (2019) 512–521, https://doi.org/10.1016/J.APPLTHERMALENG.2019.01.004.
[14] C. Wang, H. Yang, B. Nie, B. Zou, Z. Li, J. Han, L. Tong, L. Wang, Y. Ding, Discharging behavior of a shell-and-tube based thermochemical reactor for thermal energy storage: modeling and experimental validation, Int. J. Heat Mass Tran. 183 (2022), https://doi.org/10.1016/J.IJHEATMASSTRANSFER.2021.122160.
[15] J. Lin, Q. Zhao, H. Huang, H. Mao, Y. Liu, Y. Xiao, Applications of low-temperature thermochemical energy storage systems for salt hydrates based on material classification: a review, Sol. Energy 214 (2021) 149–178, https://doi.org/10.1016/J.SOLENER.2020.11.055.
[16] A. Mukherjee, A. Shankar Pujari, S.N. Shinde, U. Kashyap, L. Kumar, C. Subramaniam, S.K. Saha, Performance assessment of open thermochemical energy storage system for seasonal space heating in highly humid environment, Renew. Energy 201 (2022) 960–1481, https://doi.org/10.1016/j.renene.2022.10.075.
[17] B. Michel, P. Neveu, N. Mazet, Comparison of closed and open thermochemical processes, for long-term thermal energy storage applications, Energy 72 (2014) 702–716, https://doi.org/10.1016/J.ENERGY.2014.05.097.
[18] A. Solé, I. Martorell, L.F. Cabeza, State of the art on gas–solid thermochemical energy storage systems and reactors for building applications, Renew. Sustain. Energy Rev. 47 (2015) 386–398, https://doi.org/10.1016/J.RSER.2015.03.077.
[19] W. Li, J.J. Klemeš, Q. Wang, M. Zeng, Salt hydrate–based gas-solid thermochemical energy storage: current progress, challenges, and perspectives, Renew. Sustain. Energy Rev. 154 (2022), 111846, https://doi.org/10.1016/J.RSER.2021.111846.
[20] R.J. Clark, A. Mehrabadi, M. Farid, State of the art on salt hydrate thermochemical energy storage systems for use in building applications, J. Energy Storage 27 (2020), 101145, https://doi.org/10.1016/J.EST.2019.101145.
[21] A.H. Abedin, M.A. Rosen, Closed and open thermochemical energy storage: energy- and exergy-based comparisons, Energy 41 (2012) 83–92, https://doi.org/10.1016/J.ENERGY.2011.06.034.
[22] M. Gaeini, A.L. Rouws, J.W.O. Salari, H.A. Zondag, C.C.M. Rindt, Characterization of microencapsulated and impregnated porous host materials based on calcium chloride for thermochemical energy storage, Appl. Energy 212 (2018) 1165–1177, https://doi.org/10.1016/J.APENERGY.2017.12.131.
[23] H.A. Ousaleh, S. Said, A. Zaki, A. Faik, A. El Bouari, Silica gel/inorganic salts composites for thermochemical heat storage: improvement of energy storage density and assessment of cycling stability, Mater. Today Proc. 30 (2020) 937–941, https://doi.org/10.1016/J.MATPR.2020.04.354.
[24] Q. Wang, Y. Xie, B. Ding, G. Yu, F. Ye, C. Xu, Structure and hydration state characterizations of MgSO4-zeolite 13x composite materials for long-term thermochemical heat storage, Sol. Energy Mater. Sol. Cell. 200 (2019), 110047, https://doi.org/10.1016/J.SOLMAT.2019.110047.
[25] H. Ait Ousaleh, S. Sair, A. Zaki, A. Younes, A. Faik, A. el Bouari, Advanced experimental investigation of double hydrated salts and their composite for improved cycling stability and metal compatibility for long-term heat storage technologies, Renew. Energy 162 (2020) 447–457, https://doi.org/10.1016/J.RENENE.2020.08.085.
[26] A. Jabbari-Hichri, S. Bennici, A. Auroux, CaCl2-containing composites as thermochemical heat storage materials, Sol. Energy Mater. Sol. Cell. 172 (2017) 177–185, https://doi.org/10.1016/J.SOLMAT.2017.07.037.
[27] H. Ait Ousaleh, S. Sair, S. Mansouri, Y. Abboud, M. Zahouily, A. Faik, A. el Bouari, Enhanced inorganic salts stability using bentonite clay for high-performance and low-cost thermochemical energy storage, J. Energy Storage 49 (2022), https://doi.org/10.1016/J.EST.2022.104140.
[28] C. Agrafiotis, S. Tescari, M. Roeb, M. Schmücker, C. Sattler, Exploitation of thermochemical cycles based on solid oxide redox systems for thermochemical storage of solar heat. Part 3: cobalt oxide monolithic porous structures as integrated thermochemical reactors/heat exchangers, Sol. Energy 114 (2015) 459–475, https://doi.org/10.1016/J.SOLENER.2014.12.037.
[29] Y.N. Zhang, R.Z. Wang, Y.J. Zhao, T.X. Li, S.B. Riffat, N.M. Wajid, Development and thermochemical characterizations of vermiculite/SrBr2 composite sorbents for low-temperature heat storage, Energy 115 (2016) 120–128, https://doi.org/10.1016/J.ENERGY.2016.08.108.
[30] A. Fopah-Lele, C. Rohde, K. Neumann, T. Tietjen, T. Rönnebeck, K.E. N'Tsoukpoe, T. Osterland, O. Opel, W.K.L. Ruck, Lab-scale experiment of a closed thermochemical heat storage system including honeycomb heat exchanger, Energy 114 (2016) 225–238, https://doi.org/10.1016/j.energy.2016.08.009.
[31] D. Aydin, S.P. Casey, X. Chen, S. Riffat, Numerical and experimental analysis of a novel heat pump driven sorption storage heater, Appl. Energy 211 (2018) 954–974, https://doi.org/10.1016/J.APENERGY.2017.11.102.
[32] Y. Zhang, H. Dong, R. Wang, P. Feng, Air humidity assisted sorption thermal battery governed by reaction wave model, Energy Storage Mater. 27 (2020) 9–16, https://doi.org/10.1016/J.ENSM.2020.01.012.
[33] H. Zhang, S. Liu, A. Shukla, Y. Zou, X. Han, Y. Shen, L. Yang, P. Zhang, K. Kusakana, Thermal performance study of thermochemical reactor using net-packed method, Renew. Energy 182 (2022) 483–493, https://doi.org/10.1016/J.RENENE.2021.09.115.
[34] Z. Chen, Y. Zhang, Y. Zhang, Y. Su, S. Riffat, A study on vermiculite-based salt mixture composite materials for low-grade thermochemical adsorption heat storage, Energy 278 (2023), https://doi.org/10.1016/j.energy.2023.127986.
[35] A. Fopah Lele, F. Kuznik, H.U. Rammelberg, T. Schmidt, W.K.L. Ruck, Thermal decomposition kinetic of salt hydrates for heat storage systems, Appl. Energy 154 (2015) 447–458, https://doi.org/10.1016/J.APENERGY.2015.02.011.
[36] R. Olives, S. Mauran, A Highly Conductive Porous Medium for Solid-Gas Reactions: Effect of the Dispersed Phase on the Thermal Tortuosity, vol. 43, Transp Porous Media, 2001, pp. 377–394, https://doi.org/10.1023/A:1010780623891/METRICS.
[37] A. Malley-Ernewein, S. Lorente, Constructal design of thermochemical energy storage, Int. J. Heat Mass Tran. 130 (2019) 1299–1306, https://doi.org/10.1016/J.IJHEATMASSTRANSFER.2018.10.097.
[38] W. Li, H. Guo, M. Zeng, Q. Wang, Performance of SrBr2·6H2O based seasonal thermochemical heat storage in a novel multilayered sieve reactor, Energy Convers. Manag. 198 (2019), https://doi.org/10.1016/j.enconman.2019.111843.
[39] B. Janković, S. Mentus, M. Janković, A kinetic study of the thermal decomposition process of potassium metabisulfite: estimation of distributed reactivity model, J. Phys. Chem. Solid. 69 (2008) 1923–1933, https://doi.org/10.1016/J.JPCS.2008.01.013.
[40] W. Chen, W. Li, Y. Zhang, Analysis of thermal deposition of MgCl2·6H2O hydrated salt in the sieve-plate reactor for heat storage, Appl. Therm. Eng. 135 (2018) 95–108, https://doi.org/10.1016/J.APPLTHERMALENG.2018.02.043.
[41] Statista Research Department, UK: thermal efficiency of gas turbine stations 2021 | Stat, (n.d.). https://www.statista.com/statistics/548943/thermal-efficiency-gas-turbine-stations-uk/(accessed July 16, 2023)..
[42] A Technical Bulletin for Engineers, Contractors and Students in the Air Movement and Control Industry, Understanding Fan Efficiency Grades (FEG), 2013.
[43] D.P. Bentz, F. Zunino, D. Lootens, Chemical vs. Physical acceleration of cement hydration, Concr. Int. 38 (2016) 37. (Accessed 23 October 2023).
[44] E.A. Levitskij, Y.I. Aristov, M.M. Tokarev, V.N. Parmon, "Chemical Heat Accumulators": a new approach to accumulating low potential heat, Sol. Energy Mater. Sol. Cell. 44 (1996) 219–235, https://doi.org/10.1016/0927-0248(96)00010-4.
[45] M.W. Chase, M.W. Chase, NIST-JANAF thermochemical tables for the bromine oxides, JANAF thermochemical tables. I. Ten organic molecules related to atmospheric chemistry, J. Phys. Chem. Ref. Data 25 (1996) 475, https://doi.org/10.1063/1.555994.
[46] Y. Zhang, M. Hu, Z. Chen, Y. Su, S. Riffat, Modelling analysis of a solar-driven thermochemical energy storage unit combined with heat recovery, Renew. Energy 206 (2023) 722–737, https://doi.org/10.1016/J.RENENE.2023.02.076.